NANO LETTERS

pubs.acs.org/NanoLett Letter

Resolving Multielement Semiconductor Nanocrystals at the Atomic Level: Complete Deciphering of Domains and Order in Complex $Cu_\alpha Zn_\beta Sn_\gamma Se_\delta$ (CZTSe) Tetrapods

Huan Ren,*,¶ Yuanwei Sun,¶ Frank Hoffmann, Matthias Vandichel, Temilade E. Adegoke, Ning Liu, Conor McCarthy, Peng Gao,* and Kevin M. Ryan*

Cite This: *Nano Lett.* 2024, 24, 2125−2130 Read Online

ACCESS | Metrics & More | Article Recommendations | Supporting Information

ABSTRACT: Semiconductor nanocrystals (NCs) with high elemental and structural complexity can be engineered to tailor for electronic, photovoltaic, thermoelectric, and battery applications etc. However, this greater complexity causes ambiguity in the atomic structure understanding. This in turn hinders the mechanistic studies of nucleation and growth, the theoretical calculations of functional properties, and the capability to extend functional design across complementary semiconductor nanocrystals. Herein, we successfully deciphered the atomic arrangements of 4 different nanocrystal domains in $Cu_\alpha Zn_\beta Sn_\gamma Se_\delta$ (CZTSe) nanocrystals using crucial zone axis analysis on multiple crystals in different orientations. The results show that the essence of crystallographic progression from binary to multielemental semiconductors is actually the change of theoretical periodicity. This transition is caused by decreased symmetry in the crystal instead of previously assumed crystal deformation. We further reveal that these highly complex crystalline entities have highly ordered element arrangements as opposed to the previous understanding that their elemental orderings are random.

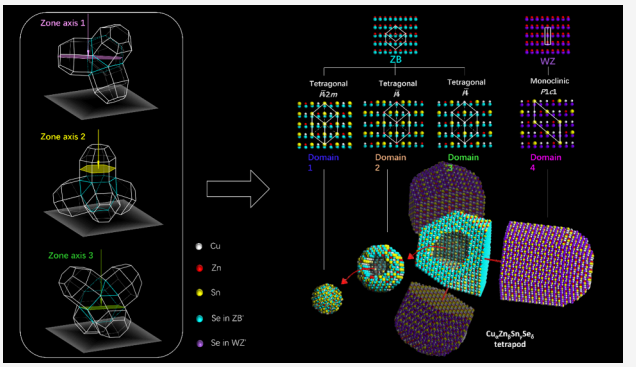

KEYWORDS: *semiconductor nanocrystal, atomic structure, Bravais lattice, semiconductor modeling, chemical ordering, first-principle calculation*

Semiconductor nanocrystals with multiple metal cations can be considered to originate from binary structures by cation substitutions (e.g $Cu_\alpha Zn_\beta Sn_\gamma Se_\delta$ from CuSe).[1,2] In binary semiconductor compositions, it is relatively straightforward to identify different ions using direct imaging analysis, such as HAADF-STEM (the intensity of the signal increases roughly monotonically with the square of the atomic number, Z[3,4]). This is because the cations and anions form separate ionic sites in the low-index and close-packing facets[3,5] (e.g., ⟨001⟩ and ⟨011⟩ in the zinc blende phase). However, the complexity of the atomic structure increases, and unit cell symmetry decreases in multiple-element crystal structures originated from binary systems. Given the random nature of sample deposition orientation, most imaging directions of multielement semiconductors will have different elements occupying the same atomic sites. These different elements aligned on the same atomic spot all contribute to the two-dimensional projection, thereby rendering these directions invalid for the chemical order analysis.

In multielement semiconductors, some chemical orders with higher order symmetry can be determined from a single zone axis, such as the [111] direction for tetragonal $I\bar{4}2m$ in $Cu_2CdSnSe_4$.[6] In another study, four interlaced $CuInS_2$ domains derived from the wurtzite crystal phase are analyzed from the equivalent wurzite [0001] direction, showing that these domains are partitioned by different chemical orderings while free from Bravais lattice boundary defects.[7] Chemical ordering analysis for these domains free from Bravais lattice boundaries are especially important because different domains are still considered as crystalline defects that largely affect a semiconductor's physical properties.[8−11] However, comparing to WZ-ZB stacking fault related defects that can be directly observed with Bravais lattice boundaries, these chemical ordering defects are more difficult to observe or analyze at an atomic level.

Herein, by imaging nanocrystals with multiple crucial zone axis orientations, we present chemical ordering analysis on highly complex quaternary element semiconductor nanocrystals with low-symmetry crystal domains.

Received: July 26, 2023
Revised: February 4, 2024
Accepted: February 7, 2024
Published: February 11, 2024

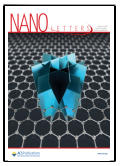

https://doi.org/10.1021/acs.nanolett.3c02810
Nano Lett. 2024, 24, 2125−2130

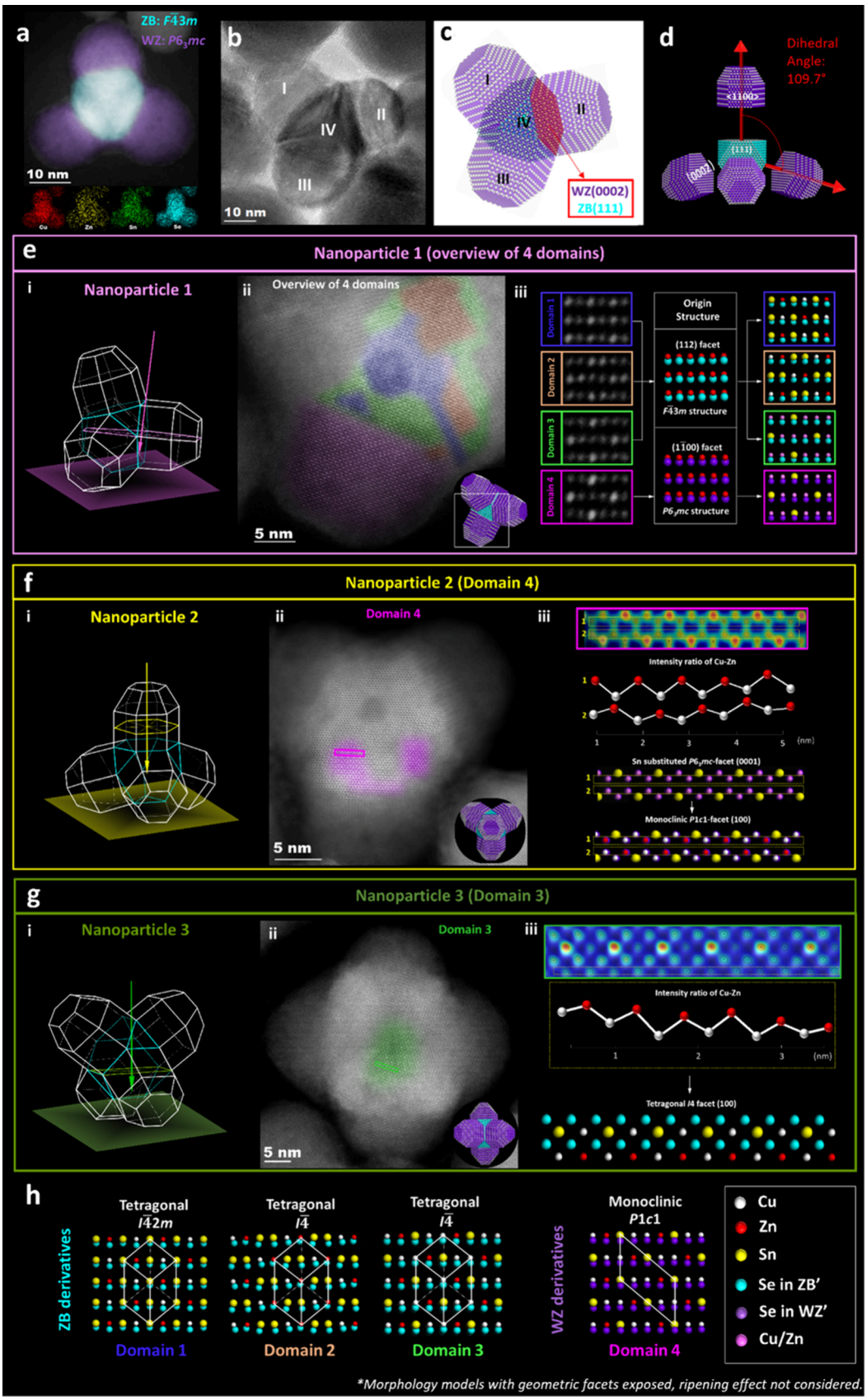

Figure 1. Atomic-level structure decipher of 4 domains in a $Cu_\alpha Zn_\beta Sn_\gamma Se_\delta$ (CZTSe) tetrapod-like nanocrystal. (a) ADF image of a single CZTSe nanocrystal with ZB (zinc blende) and WZ (wurtzite)-derived structures; bottom inset of EDX mappings with Cu red, Zn yellow, Sn green, and Se cyan. (b) TEM image of a single CZTSe tetrapod showing 3 wurtzite arms (I, II, III) and the zinc blende core (IV). (c) Corresponding structural modeling of (b) with transparent WZ structure to expose the polytypic interphases, where structures I, II, and III are wurtzite-type and structure IV is zinc blende-type. (d) Exploded view of the tetrapod NC model with dihedral angle between two arms displayed. (e) (e-i) Morphological framework

https://doi.org/10.1021/acs.nanolett.3c02810
Nano Lett. 2024, 24, 2125−2130

Figure 1. continued

indicating type 1 of nanoparticle deposition orientation on the TEM grid that facilitates imaging from equivalent ZB [112] and WZ [1$\bar{1}$00] directions; (e-ii) ADF image of a CZTSe tetrapod displaying the 4 domains with inset morphological model; (e-iii) Magnified ADF of 4 domains respectively with corresponding first-step models. (f) (f-i) Morphological framework indicating type 2 of nanoparticle deposition orientation on the TEM grid that facilitates imaging from equivalent WZ [0002] direction; (f-ii) ADF image of a CZTSe tetrapod displaying Domain 4 from a second imaging zone axis; (f-iii) Cu−Zn differentiation from equivalent WZ[0002] to determine the final atomic model of Domain 4. (g) (g-i) Morphological framework indicating type 3 of nanoparticle deposition orientation on the TEM grid that facilitates imaging from equivalent ZB [100]; (g-ii) ADF image of a CZTSe tetrapod in the deposition orientation that displays Domain 3 from a second imaging zone axis; (g-iii) Cu−Zn differentiation from equivalent ZB[100] to determine the final atomic model of Domain 3. (h), Overview of all four domains in a CZTSe tetrapod-like nanocrystal.

Morphological analysis of CZTSe tetrapod NCs[12,13] (∼48 nm) was carried out through the compilation of TEM imaging and cation−anion modeling (Figure 1a−d, Figure S1). As displayed in Figure 1a, CZTSe tetrapods have a 3D tetragonal structure with wurtzite-derived arms (original phase WZ $P6_3mc$ and a zinc-blende-derived core (original phase ZB $F\bar{4}3m$). Elements Cu (red), Zn (yellow), Sn (green), and Se (cyan) are distributed homogeneously across the whole particle with average percentages of 33.4%, 13.5%, 12.7%, and 40.4%, respectively (5 random-location analysis in Figure S2). The arms labeled I, II, and III in Figure 1b are identified as the wurtzite-type (WZ) phase and correspond to the three transparent structures I, II, and III in Figure 1c, while the core (IV) highlighted by the TEM phase contrast (Figure 1b) corresponds to quasi-tetrahedral zinc blende-type (ZB) structure IV (Figure 1c). The polytypic interphase of WZ(0002)/ZB(111) highlighted in Figure 1c is further displayed in the exploded structure view (Figure 1d) showing the ZB core and four tetrahedrally attached arms with an arm dihedral angle of 109.7°.

As shown in Figure 1e, a CZTSe tetrapod nanocrystal that has a deposition orientation of the equivalent ZB [112] and WZ [1$\bar{1}$00] was selected to present an overview of the 4 domains. From this particular zone-axis, four grain-boundary-free domains are identified across both the ZB and WZ sections (Figure 1e-i). The imaged facets of three ZB-derived structures, Domains 1, 2, and 3, are equivalent to the ZB(11$\bar{2}$) facet, while the WZ-derived Domain 4 is equivalent to WZ(1$\bar{1}$00) as shown in Figure 1e-ii. The heaviest atom type, Sn, can then be assigned according to the intensity difference at corresponding atomic sites, allowing the two origin binary element models for ZB and WZ to be updated with different periodic Sn substitutions to form intermediate Sn-substituted models (Figure 1e-iii).

From the first zone axis, Domains 1 and 2 are fully deciphered (details in Figures S3 and S4), while only the Sn positions in Domains 3 and 4 can be determined. The Cu and Zn differentiation in Domains 3 and 4 is subsequently carried out in Figure 1f,g.

Domain 4 was found in a different nanoparticle with a diffusion orientation that allows imaging from equivalent WZ[0001]. In Figure 1f−i, Cu and Zn continuously exist in the same averaged chemical environment along certain directions due to the particular atomic arrangement (the highlighted box in Figure 1f-ii). The mass centers and associated intensities of each atomic column are fitted using the optimized multiple-ellipse fitting method.[14,15] The low−high alternative pattern (overall intensity ratio Cu-Se:Zn-Se = 1:1.05; SI, Figure S6) corresponds to the alternative Cu−Se and Zn−Se atomic arrangement (theoretical Cu-Se:Zn-Se = 1:1.03) as shown in Figure 1f-iii. The intermediate Sn-substituted model from particle 1 is then rotated to WZ(0001) to match the ADF image taken from the equivalent WZ[0001]. The intermediate Sn-substituted model can then be completed with Cu and Zn substitutions, subsequently identified to be monoclinic, $P1c1$ (Figure 1f-iii).

A third CZTSe tetrapod nanocrystal orientation is used for Cu and Zn differentiation for Domain 3 (Figure 1g). From this zone axis, Cu and Zn in Domain 3 can be differentiated within the same chemical environment using a chemical analysis method similar to that described in Figure1f. The fitted overall alternative pattern intensity ratio (corresponding to a Cu:Zn) of Domain 3 is 1:1.09 (SI, Figure S5) compared to the theoretical ratio 1:1.07, confirming Domain 3 to be $I\bar{4}$, tetragonal (Figure 1g).

After the structures of all 4 domains were resolved (SI, Figure S7), their unit cell parameters were directly measured and subsequently used as preliminary input for the density functional theory (DFT) geometry optimizations (SI, Table S1−Table S5). The final real-space atomic models of the 3 core domains originating from ZB and the arm domain derived from WZ are fully deciphered with atomic precision and presented in Figure 1h.

The three tetragonal ZB-derived Domains 1, 2, and 3 share the same point group $\bar{4}$, which is a tetragonal 4-fold rotational inversion symmetry around the axis [001]. Meanwhile Domain 1 has two additional symmetry mirror planes of (100) and (010) which are parallel to the rotational inversion axis, resulting in a different space group ($I\bar{4}2m$) than the other two domains ($I\bar{4}$). For Domains 2 and 3, despite having the same space group ($I\bar{4}$), they have different stoichiometries and atomic arrangements of $CuZnSn_2Se_4$ in Domain 2 and $Cu_2ZnSnSe_4$ in Domain 3 due to the different oxidation states of Cu and Sn. As for the WZ-derivative, Domain 4 belongs to the monoclinic system with the space group, $P1c1$. Interestingly, to the best of our knowledge, the CZTSe composition has not been reported in space groups $P1c1$, $I\bar{4}2m$, or $I\bar{4}$. The discovery of new unit cells supports this method's general applicability to decipher new semiconductor compositions that have not yet been synthesized. Note that these three crucial imaging zone axes have wide rotational angles of 65.91° and 90°, which are beyond the tilting limitations in commercial double tilting holders. Therefore, we imaged different nanocrystals with the same crystalline domains and from specific orientations to further minimize the electron beam effect and eliminate instrumentation limitations. The consistency of 4 domains in distinct tetrapod nanocrystals is validated by another 2 examples shown in SI, Figure S8.

Different from our previous research on a similar CZTSe tetrapod[13] with 3 different types of Bravais lattice boundary defects, namely, polytypic, epitaxial, and heteroaxial ZB-WZ stacking faults, the 4 different domains discussed in this study are interlaced without Bravais lattice boundary defects. All 4 chemical ordering domains of different volumes with various chemical stoichiometries all contribute to the overall chemical stoichiometry, resulting in the noninteger stoichiometry,

https://doi.org/10.1021/acs.nanolett.3c02810
Nano Lett. 2024, 24, 2125−2130

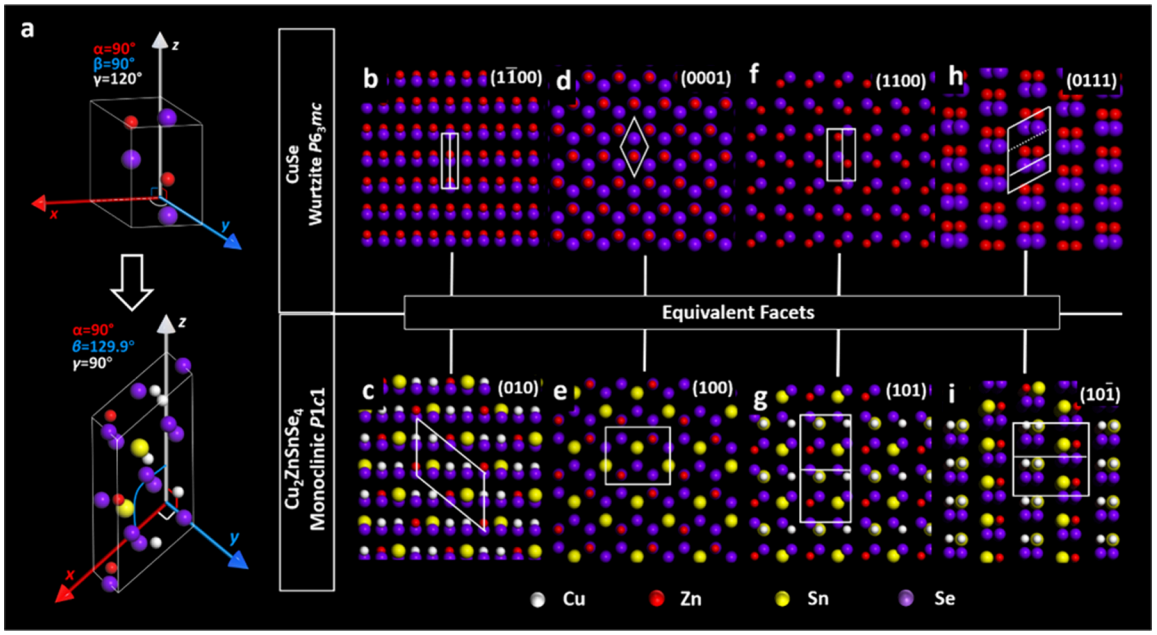

Figure 2. Structural equivalency between low-symmetry structures and their ZB and WZ origins (high-ighted shapes in (b)−(i) are unit cell projections in respective structures from the viewing direction). (a) Transition from WZ ($P6_3mc$) Cu(II)Se to monoclinic ($P1c1$) $Cu_2ZnSnSe_4$. (b) Crystal facet WZ($1\bar{1}00$). (c) Equivalent facet of (b) in the monoclinic structure. (d) Crystal facet WZ(0001). (e) Equivalent facet of (d) in monoclinic structure. (f) Crystal facet WZ(1100). (g) Equivalent facet of (f) in the monoclinic structure. (h) Crystal facet WZ(1100). (i) Equivalent facet of (h) in monoclinic structure.

$Cu_{2.6}Zn_{1.1}SnSe_{3.2}$ (Figure S2). A further outcome of this atomically precise structural study is a new interpretation that complex chalcogenide nanocrystals are in fact highly ordered crystalline entities from periodic element substitutions, as opposed to the previous understanding that they are the results of random cationic substitutions[9,16−22] (e.g., $CuSnSe_2$ resulting from Sn randomly replacing Cu in CuSe).

Despite the high complexity in multielement nanocrystals, in Figure 2, certain correlations are established between binary high-symmetry and multielement low-symmetry systems, allowing us to interpret these structures. Taking the progression from Cu(II)Se[23] ($P6_3mc$, Figure 2a-top) to $Cu_2ZnSnSe_4$ ($P1c1$, Figure 2a-bottom), for example, the crystal structure changes from hexagonal to monoclinic with the increase of unit cell volume ($V(P6_3mc)$ = 91.22 Å^3 to $V(P1c1)$ = 392.82 Å^3). Even though this progression from binary to quaternary entails complete changes of the coordinate system and unit cell shape, a certain structural equivalency still exists despite the seemingly drastic transition. As shown in Figure 2b,c, the derivative monoclinic structure is the result of periodic substitutions of Cu with Zn and Sn. In Figure 2d,e, the characteristic hexagonal atomic arrangement is unchanged upon incorporation of more elements (atomic position distortion upon substitutions of different elements neglected). Similar equivalent facets are observed in Figure 2f,g and Figure 2h,i. In summary, as shown in the highlighted unit cell projections from Figure 2b to Figure 2i, when new elements are incorporated into the structure, the unit cell volume increases and symmetry decreases to accommodate more coordinates of various elements. Essentially, this seemingly significant crystal structure change is the boundary change of the theoretical minimum crystallographic periodicity instead of previously assumed "crystal structure deformation".[24,25]

CONCLUSION

Using equivalency between low- and high-symmetry semiconductor structures, the unit cells of five domains in highly complex semiconductor crystals are deciphered from three nanocrystals with orientations that facilitate crucial zone axis imaging. It provides a highly effective chemical ordering deciphering method for complex semiconductor domains with multielements and low crystallographic symmetry. This in turn gives direct guidance to first-principles calculations of semiconductor structures and thereby offers new insights from the mechanisms underlying their synthesis to unlocking the basis for their physical properties.

ASSOCIATED CONTENT

Supporting Information

The Supporting Information is available free of charge at https://pubs.acs.org/doi/10.1021/acs.nanolett.3c02810.

I, Material and methods; II, Morphological analysis; III, Atomic level decipher; and IV, Coordination shift upon different element incorporation (PDF)
Crystallographic information file for Domain 1 (CIF)
Crystallographic information file for Domain 2 (CIF)
Crystallographic information file for Domain 3 (CIF)
Crystallographic information file for Domain 4 (CIF)

AUTHOR INFORMATION

Corresponding Authors

Huan Ren − *Department of Chemical Sciences and Bernal Institute, University of Limerick, Limerick V94 T9PX, Ireland; Material Science and Engineering, National University of Singapore, 117557, Singapore;* orcid.org/0000-0002-4030-6210; Email: huanrennanotech@outlook.com

Peng Gao − *International Center for Quantum Materials and Electron Microscopy Laboratory, School of Physics, Peking*

https://doi.org/10.1021/acs.nanolett.3c02810
Nano Lett. 2024, 24, 2125−2130

University, Beijing 100871, P.R. China; Email: p-gao@pku.edu.cn

Kevin M. Ryan − *Department of Chemical Sciences and Bernal Institute, University of Limerick, Limerick V94 T9PX, Ireland*; orcid.org/0000-0003-3670-8505; Email: kevin.m.ryan@ul.ie

Authors

Yuanwei Sun − *International Center for Quantum Materials and Electron Microscopy Laboratory, School of Physics, Peking University, Beijing 100871, P.R. China; Medical Science and Technology Innovation Center, Shandong First Medical University & Shandong Academy of Medical Sciences, Jinan, Shandong 250117, P.R. China*

Frank Hoffmann − *Department of Chemistry, Institute of Inorganic and Applied Chemistry, University of Hamburg, Hamburg 20148, Germany*; orcid.org/0000-0002-6060-838X

Matthias Vandichel − *Department of Chemical Sciences and Bernal Institute, University of Limerick, Limerick V94 T9PX, Ireland*; orcid.org/0000-0003-1592-0726

Temilade E. Adegoke − *Department of Chemical Sciences and Bernal Institute, University of Limerick, Limerick V94 T9PX, Ireland*; orcid.org/0000-0001-5201-4410

Ning Liu − *Department of Physics and Bernal Institute, University of Limerick, Limerick V94 T9PX, Ireland*; orcid.org/0000-0003-1164-6387

Conor McCarthy − *Confirm Centre & Bernal Institute, School of Engineering, University of Limerick, Limerick V94 T9PX, Ireland*

Complete contact information is available at: https://pubs.acs.org/10.1021/acs.nanolett.3c02810

Author Contributions

¶(H.R. and Y.S.) These authors have made equal contributions.

Notes

The authors declare no competing financial interest.

■ ACKNOWLEDGMENTS

This project is supported by Irish Research Council (IRC) under Grant No. IRCLA/2017/285. K.M.R. acknowledges Science Foundation Ireland (SFI) under the Principal Investigator Program under Contract No. 16/IA/4629 and under Grant No. SFI 16/M-ERA/3419. K.M.R. further acknowledges IRCLA/2017/285 and SFI Research Centres MaREI, AMBER, and CONFIRM 12/RC/2278_P2, 12/RC/2302_P2, and 16/RC/3918.

■ REFERENCES

(1) Stroyuk, O.; Raevskaya, A.; Gaponik, N. Solar Light Harvesting with Multinary Metal Chalcogenide Nanocrystals. *Chem. Soc. Rev.* **2018**, *47* (14), 5354−5422.

(2) Regulacio, M. D.; Han, M.-Y. Multinary I-III-VI_2 and I_2-II-IV-VI_4 Semiconductor Nanostructures for Photocatalytic Applications. *Acc. Chem. Res.* **2016**, *49* (3), 511−519.

(3) Krivanek, O. L.; Chisholm, M. F.; Nicolosi, V.; Pennycook, T. J.; Corbin, G. J.; Dellby, N.; Murfitt, M. F.; Own, C. S.; Szilagyi, Z. S.; Oxley, M. P.; et al. Atom-by-Atom Structural and Chemical Analysis by Annular Dark-Field Electron Microscopy. *Nature* **2010**, *464* (7288), 571.

(4) Pennycook, S.; Jesson, D. High-Resolution Z-contrast Imaging of Crystals. *Ultramicroscopy* **1991**, *37* (1−4), 14−38.

(5) Manna, L.; Wang, L. W.; Cingolani, R.; Alivisatos, A. P. First-Principles Modeling of Unpassivated and Surfactant-Passivated Bulk Facets of Wurtzite CdSe: A Model System for Studying the Anisotropic Growth of CdSe Nanocrystals. *J. Phys. Chem. B* **2005**, *109* (13), 6183−6192.

(6) Zamani, R. R.; Ibanez, M.; Luysberg, M.; Garcia-Castello, N.; Houben, L.; Prades, J. D.; Grillo, V.; Dunin-Borkowski, R. E.; Morante, J. R.; Cabot, A.; et al. Polarity-Driven Polytypic Branching in Cu-based Quaternary Chalcogenide Nanostructures. *ACS Nano* **2014**, *8* (3), 2290−2301.

(7) Shen, X.; Hernández-Pagan, E. A.; Zhou, W.; Puzyrev, Y. S.; Idrobo, J.-C.; Macdonald, J. E.; Pennycook, S. J.; Pantelides, S. T. Interlaced Crystals Having a Perfect Bravais Lattice and Complex Chemical Order Revealed by Real-Space Crystallography. *Nat. Commun.* **2014**, *5*, 5431.

(8) Norris, D. J.; Efros, A. L.; Erwin, S. C. Doped Nanocrystals. *Science* **2008**, *319* (5871), 1776−1779.

(9) Bao, L.; Zang, J.; Wang, G.; Li, X. Atomic-Scale Imaging of Cation Ordering in Inverse Spinel Zn_2SnO_4 Nanowires. *Nano Lett.* **2014**, *14* (11), 6505−6509.

(10) Liu, Z.; Zhong, Y.; Shafei, I.; Borman, R.; Jeong, S.; Chen, J.; Losovyj, Y.; Gao, X.; Li, N.; Du, Y.; et al. Tuning Infrared Plasmon Resonances in Doped Metal-Oxide Nanocrystals Through Cation-Exchange Reactions. *Nat. Commun.* **2019**, *10* (1), 1394.

(11) Kriegel, I.; Scotognella, F.; Manna, L. Plasmonic Doped Semiconductor Nanocrystals: Properties, Fabrication, Applications and Perspectives. *Phys. Rep.* **2017**, *674*, 1−52.

(12) Ren, H.; Li, Z.; Sun, Y.; Gao, P.; McCarthy, C.; Liu, N.; Xu, H.; Ryan, K. M. Precursor-Mediated Linear-and Branched-Polytypism Control in $Cu_\alpha Zn_\beta Sn_\gamma Se_\delta$ Colloidal Nanocrystals Using a Dual-injection Method. *Chem. Mater.* **2020**, *32* (17), 7254−7262.

(13) Ren, H.; Sun, Y.; Gao, P.; Ryan, K. M. Direct Observation of the Conventional Epitaxial and Novel Heteroaxial ZB-WZ Stacking Faults. *Crys. Growth Des.* **2023**, *23* (8), 5384−5388.

(14) Zhang, Q.; Zhang, L.; Jin, C.; Wang, Y.; Lin, F. CalAtom: A Software for Quantitatively Analysing Atomic Columns in a Transmission Electron Microscope Image. *Ultramicroscopy* **2019**, *202*, 114−120.

(15) Zhang, Q.; Jin, C.; Xu, H.; Zhang, L.; Ren, X.; Ouyang, Y.; Wang, X.; Yue, X.; Lin, F. Multiple-Ellipse Fitting Method to Precisely Measure the Positions of Atomic Columns in a Transmission Electron Microscope Image. *Micron* **2018**, *113*, 99−104.

(16) Chen, S.; Gong, X.; Walsh, A.; Wei, S.-H. Electronic Structure and Stability of Quaternary Chalcogenide Semiconductors Derived from Cation Cross-Substitution of II-VI and I-III-VI_2 Compounds. *Phys. Rev. B* **2009**, *79* (16), No. 165211.

(17) Lu, X.; Zhuang, Z.; Peng, Q.; Li, Y. Wurtzite Cu_2ZnSnS_4 Nanocrystals: a Novel Quaternary Semiconductor. *Chem. Commun.* **2011**, *47* (11), 3141−3143.

(18) Zhang, X.; Bao, N.; Ramasamy, K.; Wang, Y.-H. A.; Wang, Y.; Lin, B.; Gupta, A. Crystal Phase-Controlled Synthesis of Cu_2FeSnS_4 Nanocrystals with a Band Gap of Around 1.5 eV. *Chem. Commun.* **2012**, *48* (41), 4956−4958.

(19) Rost, C. M.; Sachet, E.; Borman, T.; Moballegh, A.; Dickey, E. C.; Hou, D.; Jones, J. L.; Curtarolo, S.; Maria, J.-P. Entropy-Stabilized Oxides. *Nat. Commun.* **2015**, *6*, 8485.

(20) Wang, F.; Han, Y.; Lim, C. S.; Lu, Y.; Wang, J.; Xu, J.; Chen, H.; Zhang, C.; Hong, M.; Liu, X. Simultaneous Phase and Size Control of Upconversion Nanocrystals Through Lanthanide Doping. *Nature* **2010**, *463* (7284), 1061−1065.

(21) Buannic, L.; Blanc, F. d. r.; Middlemiss, D. S.; Grey, C. P. Probing Cation and Vacancy Ordering in the Dry and Hydrated Yttrium-Substituted $BaSnO_3$ Perovskite by NMR Spectroscopy and First Principles Calculations: Implications for Proton Mobility. *J. Am. Chem. Soc.* **2012**, *134* (35), 14483−14498.

(22) Ren, H.; Wang, M.; Li, Z.; Laffir, F.; Brennan, G.; Sun, Y.; Stokes, K.; Geaney, H.; O'Reilly, E. J.; Gao, P.; et al. Synthesis and Characterization of $CuZnSe_2$ Nanocrystals in Wurtzite, Zinc Blende and Core-Shell Polytypes. *Chem. Mater.* **2019**, *31* (24), 10085−10093.

(23) Berry, L. The Crystal Structure of Covellite, Cuse and Klockmannite, Cuse. *Am. Mineral.* **1954**, *39* (5−6), 504−509.

(24) Boccara, N. Second-Order Phase Transitions Characterized by a Deformation of the Unit cell. *Ann. Phys.* **1968**, *47* (1), 40−64.
(25) Son, D. H.; Hughes, S. M.; Yin, Y.; Alivisatos, A. P. Cation Exchange Reactions in Ionic Nanocrystals. *Science* **2004**, *306* (5698), 1009−1012.

https://doi.org/10.1021/acs.nanolett.3c02810
Nano Lett. 2024, 24, 2125−2130